MNRAS **458,** 1990–1998 (2016)
Advance Access publication 2016 February 22
doi:10.1093/mnras/stw403

Widespread deuteration across the IRDC G035.39−00.33

A. T. Barnes,[1,2★] S. Kong,[3] J. C. Tan,[3,4] J. D. Henshaw,[1] P. Caselli,[5] I. Jiménez-Serra[6] and F. Fontani[7]

[1]*Astrophysics Research Institute, Liverpool John Moores University, 146 Brownlow Hill, Liverpool L3 5RF, UK*
[2]*School of Physics and Astronomy, University of Leeds, LS2 9JT Leeds, UK*
[3]*Department of Astronomy, University of Florida, Gainesville, FL 32611, USA*
[4]*Department of Physics, University of Florida, Gainesville, FL 32611, USA*
[5]*Max-Plank-Institute for Extraterrestrial Physics (MPE), Giessenbachstrasse 1, D-85748 Garching, Germany*
[6]*Department of Physics and Astronomy, University College London, 132 Hampstead Road, London NW1 2PS, UK*
[7]*INAF – Osservatorio Astrofisico di Arcetri, L.go E. Fermi 5, I-50125 Firenze, Italy*

Accepted 2016 February 18. Received 2016 February 15; in original form 2015 October 19

ABSTRACT

Infrared Dark Clouds (IRDCs) are cold, dense regions that are usually found within Giant Molecular Clouds. Ongoing star formation within IRDCs is typically still deeply embedded within the surrounding molecular gas. Characterizing the properties of relatively quiescent IRDCs may therefore help us to understand the earliest phases of the star formation process. Studies of local molecular clouds have revealed that deuterated species are enhanced in the earliest phases of star formation. In this paper, we test this towards IRDC G035.39−00.33. We present an 80 arcsec by 140 arcsec map of the $J = 2 \rightarrow 1$ transition of N_2D^+, obtained with the Institut de Radioastronomie Millimétrique 30 m telescope telescope. We find that N_2D^+ is widespread throughout G035.39−00.33. Complementary observations of N_2H^+ $(1 - 0)$ are used to estimate the deuterium fraction, $D_{\rm frac}^{N_2H^+} \equiv N(N_2D^+)/N(N_2H^+)$. We report a mean $D_{\rm frac}^{N_2H^+} = 0.04 \pm 0.01$, with a maximum of $D_{\rm frac}^{N_2H^+} = 0.09 \pm 0.02$. The mean deuterium fraction is ∼3 orders of magnitude greater than the interstellar [D]/[H] ratio. High angular resolution observations are required to exclude beam dilution effects of compact deuterated cores. Using chemical modelling, we find that the average observed values of $D_{\rm frac}^{N_2H^+}$ are in agreement with an equilibrium deuterium fraction, given the general properties of the cloud. This implies that the IRDC is at least ∼3 Myr old, which is ∼8 times longer than the mean free-fall time of the observed deuterated region.

Key words: stars: formation – ISM: clouds – ISM: molecules.

1 INTRODUCTION

Infrared Dark Clouds (IRDCs) are regions of cold ($T < 25$K; e.g. Ragan, Bergin & Wilner 2011) and dense ($n(H_2) \geq 10^{3-4}$ cm^{-3}; e.g. Hernandez et al. 2011; Butler & Tan 2012) gas, the most massive and dense of which have the potential to host the earliest stages of massive star and star cluster formation (Tan et al. 2014). Thus to understand these processes it is important to study the physical and chemical properties of IRDCs.

In such cold and dense environments, some molecules 'freeze-out' on to the surfaces of dust grains forming icy mantles. Most notably CO is found to be highly depleted towards dense clouds within IRDCs (e.g. Fontani et al. 2012b; Giannetti et al. 2014), with line of sight CO depletion factors, f_D, of a few being reported towards the IRDC, G035.39−00.33 (i.e. the observed gas phase abundance of CO is a few times smaller than expected in the case of no depletion; Hernandez et al. 2011).

Unlike CO, N-bearing species, in particular NH_3 and N_2H^+, better trace dense and cold gas (e.g. Caselli et al. 1999; Bergin et al. 2002; Bergin & Tafalla 2007; di Francesco et al. 2007; Fontani et al. 2012a,c). This is due to the fact that CO, largely frozen out, is unable to effectively destroy their molecular ion precursors (such as NH^+ and H_3^+), and hence less efficiently convert N_2H^+ into HCO^+. CO depletion, therefore, can boost the formation of nitrogen-bearing species. Furthermore, in the cold and dense environments of molecular clouds, abundances of deuterated nitrogen-bearing molecules are enhanced, as the formation rates of the deuterated forms of H_3^+ also increase with CO freeze-out (e.g. Dalgarno & Lepp 1984; Walmsley, Flower & Pineau des Forêts 2004). These molecules are produced mainly by the exothermic proton–deuteron exchange

★ E-mail: A.T.Barnes@2014.ljmu.ac.uk

reaction (for para-state reactants and products; Pagani, Salez & Wannier 1992):

$$H_3^+ + HD \rightarrow H_2D^+ + H_2 + \Delta E, \quad (1)$$

where $\Delta E = 232$ K (Millar, Bennett & Herbst 1989). For significant levels of CO depletion, temperatures below 30 K, and for an ortho-to-para H_2 ratio less than ∼0.1–0.01 (e.g. Sipilä, Caselli & Harju 2013; Kong et al. 2015a), this reaction proceeds from left to right, producing an excess of H_2D^+ and an abundance ratio ($[H_2D^+]/[H_3^+]$) orders of magnitude larger than the interstellar [D]/[H] ratio (∼1.5×10^{-5}; e.g. Oliveira et al. 2003). Once the deuterated isotopologues of H_3^+ have formed, they can easily cede a deuteron to other neutral species and enhance their abundances. For example, the reactions of deuterated isotopologues of H_3^+ with N_2 can produce N_2D^+ increasing the deuteration fraction of N_2H^+, $D_{frac}^{N_2H^+}$ (we adopt the notation used by Kong et al. 2015a, where the non-deuterated counterpart is shown in superscript).

Measurements of $D_{frac}^{N_2H^+}$ towards low-mass cores range between ≃0.1 and 0.7 (e.g. Crapsi et al. 2004, 2005; Belloche et al. 2006; Pagani et al. 2007; Friesen et al. 2010; Bourke et al. 2012; Friesen, Kirk & Shirley 2013). For a sample of potential high-mass star-forming regions, Fontani et al. (2006) found $D_{frac}^{N_2H^+} \simeq 0.015$. Miettinen, Hennemann & Linz (2011) found $D_{frac}^{N_2H^+} \simeq 0.002$–$0.028$ towards massive clumps within several IRDCs, while deuterium fractions as high as in low-mass pre-stellar cores have been observed towards massive starless clumps/cores embedded in quiescent IRDCs (Fontani et al. 2011).

This paper focusses on the massive (17,000 ± 5000 $M_\odot$; Kainulainen & Tan 2013), filamentary IRDC, G035.39−00.33 which resides at a distance of 2.9 ± 0.5 kpc (Simon et al. 2006).[1] This IRDC was first identified as having the potential to host massive cluster formation by Rathborne, Jackson & Simon (2006). The extinction mapping of Butler & Tan (2012) found several high-mass surface density 'cores' within G035.39−00.33, most notably the 'H6' region which contains ∼70 $M_\odot$ of material within a radius of ∼0.25 pc. In recent years this IRDC has been the subject of an in-depth analysis, which has focused on: large-scale shocks traced by SiO emission (Jiménez-Serra et al. 2010, Paper I), widespread CO depletion (Hernandez et al. 2011, Paper II), the virial state of the cloud (Hernandez et al. 2012, Paper III) and the kinematics of the low and high density gas and the excitation conditions in the cloud at varying scales (Henshaw et al. 2013; Jiménez-Serra et al. 2014; Henshaw et al. 2014, Paper IV; Paper V; Paper VI, respectively). As widespread CO depletion has been found in G035.39−00.33, this cloud is an ideal candidate to also exhibit widespread deuteration. This paper presents Institut de Radioastronomie Millimétrique 30 m telescope (IRAM-30 m) N_2D^+ (2–1) observations of G035.39−00.33, with the aim of estimating the column density and deuterium fraction, and ultimately finding the evolutionary state of the cloud.

2 OBSERVATIONS

The N_2D^+ (2–1) observations were carried out throughout 2009 August with the IRAM-30 m at Pico Veleta, Spain. The large-scale images were obtained in the On-The-Fly (OTF) mapping mode. The central coordinates of the maps are α(J2000) = $18^h57^m08^s$, δ(J2000) = 02°10′30″ (l = 35.°517, b = −0.°274). The off-source position used was (300″, 0″; in relative coordinates). The EMIR receivers were used. The VErsatile SPectrometer Assembly (VESPA) provided a spectral resolution at 156 kHz (equivalent to 0.3 km s^{-1}) at the frequency of the N_2D^+(2–1) line (main hyperfine component frequency 154217.1805 MHz; Dore et al. 2004). The data were converted into main beam brightness temperature, T_{MB}, from antenna temperature, T_A^*, by using the beam and forward efficiencies shown in Table 1. Saturn was observed to calculate the focus, and pointing was checked every ∼2 hr on G34.3+0.2. The data were calibrated with the chopper-wheel technique (Kutner & Ulich 1981), with a calibration uncertainty of ∼20 per cent. Information on the beam sizes, frequencies, velocity resolutions are summarized in Table 1.

GILDAS[2] packages CLASS and MAPPING were used to post-process the data. This included subtracting a single-order polynomial function to produce a flat baseline, and convolving the OTF-data with a Gaussian kernel, increasing the signal- to-noise ratio, and allowing us to resample the data on to a regularly spaced grid. The absolute angular resolution of the IRAM-30 m antenna at the frequency of the J = 2 → 1 transition of N_2D^+ is ∼16 arcsec. Throughout this work, all line data are spatially smoothed to achieve an effective angular resolution of ∼27 arcsec, with a pixel spacing of 13.5 arcsec, to allow comparison with the N_2H^+ data.

We utilize the N_2H^+ (1 − 0) map from Paper IV (see this paper for more information on the N_2H^+ observations), CO depletion map of Paper III, and the mass surface density map from Kainulainen & Tan (2013).

Table 1. Frequency (MHz), velocity resolution, beam size, and beam and forward efficiency for the observed transitions. Note that the forward and beam efficiencies have been extrapolated from the telescope specified values to the transition frequencies[1].

Transition	ν (MHz)	Δv_{res} (km s^{-1})	Beam size[1] (arcsec)	Beam[1] Eff	Forward[1] Eff
N_2D^+ (2–1)	154217.18[a]	0.31	16	0.66	0.93
N_2H^+ (1–0)[b]	93176.25[c]	0.61	26	0.74	0.95
$C^{18}O$ (1–0)	109782.17[d]	0.053	22	0.73	0.97

Notes. [1]http://www.iram.es/IRAMES/ mainWiki/Iram30mEfficiencies.
[a]Main hyperfine component, J = 2–1, F_1= 3–2, F = 4–3, from Dore et al. (2004), with the central frequency updated to the value found in the CDMS catalogue (http://www.astro.uni-koeln.de/cdms/catalog).
[b]Data from Paper IV.
[c]Isolated hyperfine component, J = 1–0, F_1= 0–1, F= 1–2, from Pagani, Daniel & Dubernet (2009b).
[d]Cazzoli, Puzzarini & Lapinov (2003).

3 RESULTS

Fig. 1 presents the averaged spectrum for the mapped region, and some example spectra taken at positions of high integrated intensity (see Fig. 2). All emission above a 3σ level of ∼0.21 K km s^{-1}($\sigma = \sigma_{RMS}\ \Delta v_{res} \sqrt{N_{ch}}$; where σ_{RMS} is the root mean square noise of the spectrum in K, N_{ch} is the number of channels and Δv_{res} is the velocity resolution in km s^{-1}), is seen within a velocity range of 40–50 km s^{-1}. This range is comparable to that found by the previously mentioned works on this cloud, and

[1] Following Paper II, we adopt the kinematic distances of Simon et al. (2006), who assumed the Clemens (1985) rotation curve. This leads to a distance of 2.9 kpc for G035.39−00.33. The uncertainties in this distance are likely to be of the order of 0.5 kpc, which could result, for example, from line-of-sight non-circular motions of ∼8 km s^{-1}.

[2] see https://www.iram.fr/IRAMFR/GILDAS/

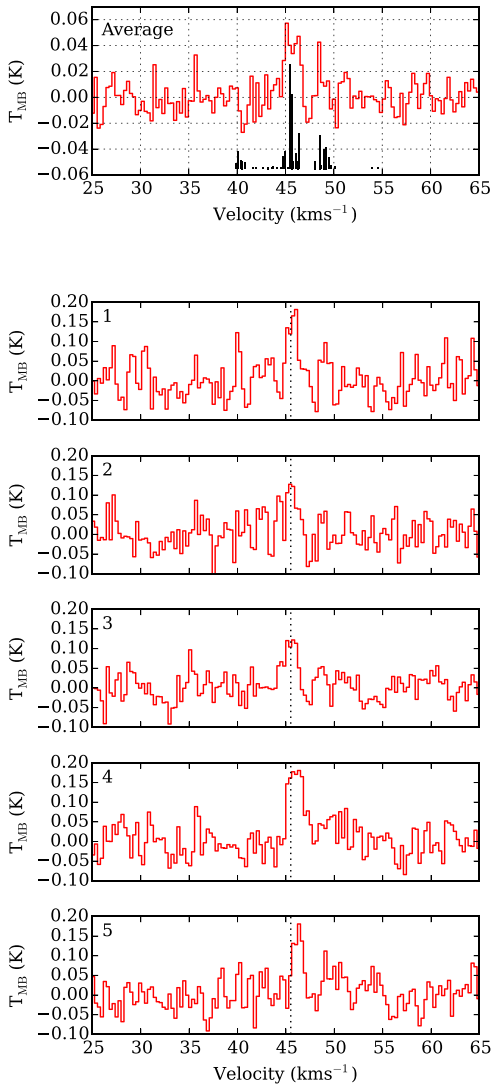

Figure 1. The upper panel shows the average spectrum of N_2D^+ $(2-1)$ for all positions (red histogram). The vertical black lines below the spectrum indicate the positions and relative strengths of all the hyperfine components of the N_2D^+ $(2-1)$ transition (Dore et al. 2004), assuming a rest velocity of 45.5 km s^{-1}. The lower panels are example spectra taken from positions of high integrated intensity, represented as the boxes on Fig. 2. The dotted lines represent a velocity of 45.5 km s^{-1}.

therefore we can be confident that the observed N_2D^+ emission is associated with G035.39−00.33.

Each spectrum has been inspected by-eye for the presence of multiple velocity components previously identified in N_2H^+ and $C^{18}O$ emission (Paper IV; with mean N_2H^+ emission velocities of 42.95 ± 0.17 km s^{-1}, 45.63 ± 0.03 km s^{-1}, and 46.77 ± 0.06 km s^{-1}). However, evidence of only one component, centred at ∼46 km s^{-1} was found in the N_2D^+ data. Unlike the N_2H^+ $(1-0)$ line, where one of the seven hyperfine components is isolated, N_2D^+ $(2-1)$ possesses no isolated hyperfine components; the line is a blend of 40 hyperfine components, spread across a velocity range of 14.6 km s^{-1} (as shown in Fig. 1, upper panel). This, as well as linewidths of ∼1 km s^{-1} (i.e. similar to those of N_2H^+ $(1-0)$; Paper IV), makes the identification of multiple velocity components very difficult.

Fig. 2 presents a map of the N_2D^+ $(2-1)$ emission integrated between 40 and 50 km s^{-1}. The integrated intensity contours are overlaid on the mass surface density map of Kainulainen & Tan (2013), and superimposed are the positions of the massive cores first identified by Rathborne et al. (2006) in millimetre continuum emission, which have been repositioned to the mid-infrared extinction peaks by Butler & Tan (2012). In Fig. 2, we also show the location and strength of the 4.5 μm emission ('green fuzzies'; Chambers et al. 2009), and the 8 μm and 24 μm (Carey et al. 2009). The N_2D^+ emission is concentrated towards the 'H6' region, and the south, near H2, H3, H4, and H5 'core' regions. However, when considering the 2σ emission level there is evidence to suggest that the emission is extended across a large portion of the cloud.

4 ANALYSIS

4.1 Column density

The column densities are calculated from the integrated intensity of the N_2D^+ (2–1) line, following the procedure outlined in Caselli et al. (2002b) for optically thin emission. This is a reasonable assumption based on the relatively faint lines detected across the cloud. We assume a constant excitation temperature of $T_{ex} \sim 4.5$ K (equivalent to the mean T_{ex} derived from the N_2H^+ observations; Paper IV). Note, that ranging the T_{ex} between 4 and 20 K would cause the column density to vary by $N(N_2D^+)^{+30\,\text{per cent}}_{-60\,\text{per cent}}$.

The mean beam-averaged column density is $N(N_2D^+) = 6.2 \pm 1.4 \times 10^{11}$ cm^{-2}, when imposing a three sigma threshold on the N_2D^+ (2–1) emission. The maximum beam-averaged column density of N_2D^+ is found towards the H6 region, with a value of $N(N_2D^+) = 8.0 \pm 1.4 \times 10^{11}$ cm^{-2}.

4.2 Deuterium fraction

The N_2D^+ to N_2H^+ column density ratio is used to define the deuterium fraction across the mapped region. Fig. 3 shows the deuterium fraction for positions where the emission of both N_2D^+ and N_2H^+ is detected above a 2σ (cross hatched), above a 2.5σ (hatched), and above a 3σ (no hatch) level. We find values of the deuteration fractions larger than 0.01 widespread throughout the cloud, with the highest values found towards the north.

Taking into account only the emission above 3σ, the mean beam-averaged deuterium fraction across G035.39−00.33 is $D_{frac}^{N_2H^+} = 0.04 \pm 0.01$. The maximum value is found north of the 'H6' region (at α(J2000) = $18^h57^m09^s$, δ(J2000) = 02°11′39″), with a value of $D_{frac}^{N_2H^+} = 0.09 \pm 0.02$. Note that varying the excitation temperature for both N_2H^+ and N_2D^+ between 4 and 20 K would cause would cause a change of $D_{frac}^{N_2H^+\,+15\,\text{per cent}}_{-55\,\text{per cent}}$.

5 DISCUSSION

5.1 G035.39−00.33 in the context of other star-forming regions

As in low-mass star-forming regions, the deuterium fraction of massive star-forming regions is believed to be a good evolutionary tracer (e.g. Fontani et al. 2011). However, the exact boundaries to define an evolutionary state are still poorly understood. To show this, plotted on Fig. 4 is the column densities of N_2D^+ and N_2H^+ found in this work, and for various other high-mass (Fontani et al. 2006, 2011; Miettinen et al. 2011; Gerner et al. 2015; Kong et al.

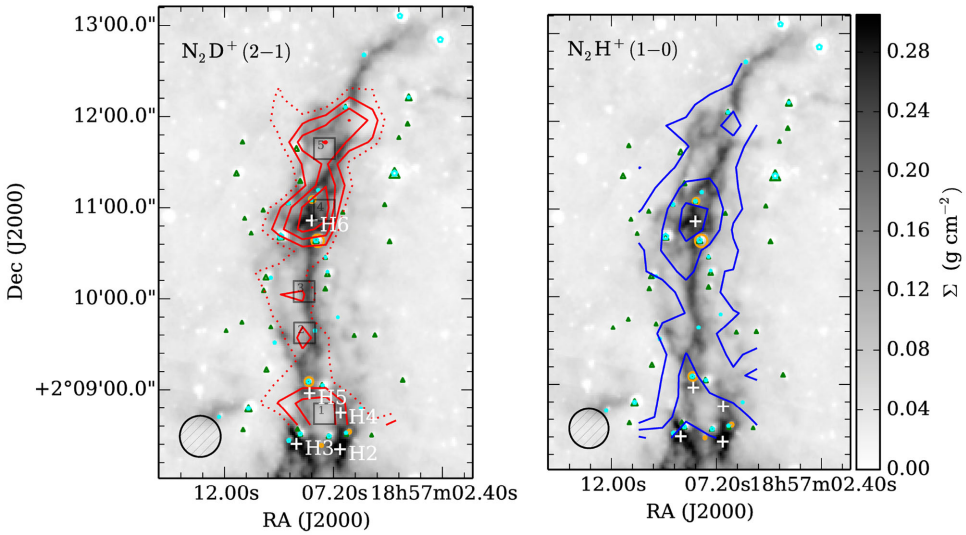

Figure 2. The left-hand panel shows the integrated intensity map of N_2D^+ (2–1) emission seen in contours of 2σ (dotted contour), 3σ, 4σ, and 5σ; where $\sigma = 0.07$ K km s^{-1}. Overlaid are boxes which represent the positions of the spectra shown in Fig. 1. The right-hand panel shows the integrated intensity contours of the N_2H^+ $(1-0)$ emission, data taken from Paper IV; contours are 5σ, 10σ, and 15σ, where $\sigma \sim 0.11$ K km s^{-1}. Each contour map is overlaid on the mass surface density map (Kainulainen & Tan 2013). White crosses indicate the positions of the massive cores (Butler & Tan 2012), and the symbols indicate the positions of the 8 μm and 24 μm sources (green triangles and cyan pentagons, respectively; Carey et al. 2009), and the 4.5 μm extended emission sources or 'green fuzzies' (orange circles; Chambers et al. 2009). The size of each source represents the strength of the emission (Paper I). The hatched circle represents the effective spatial resolution of the observations (after smoothing).

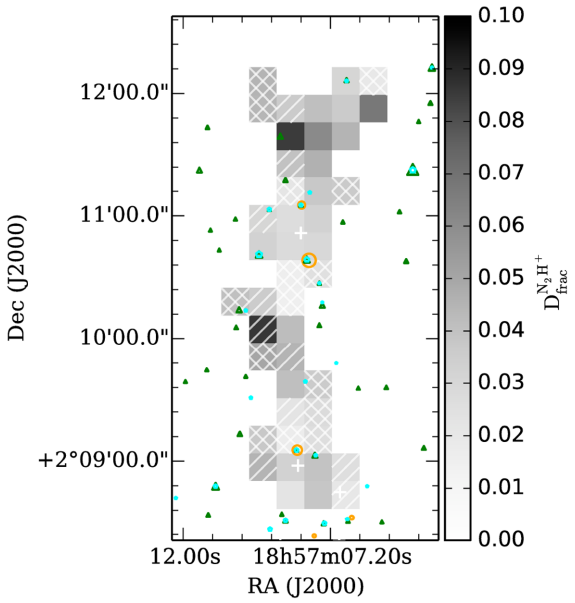

Figure 3. A map of the deuterium fraction. This map includes the emission of both N_2D^+ and N_2H^+ detected at a 2σ level shown cross hatched, above a 2.5σ level shown hatched, and above 3σ with no hatch. Symbols are identical to those in Fig. 2.

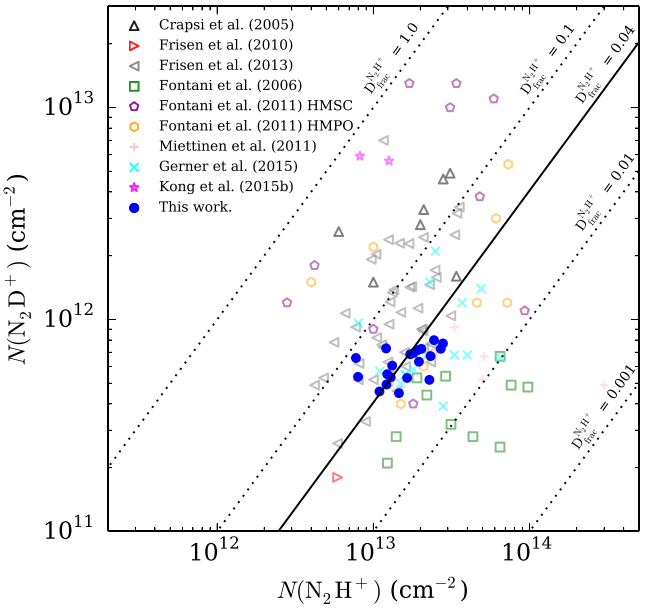

Figure 4. Column density of N_2H^+ as a function of the column density of N_2D^+, for the values found in this work and those found within the literature; triangles represent the low-mass star-forming regions, the additional shapes represent high-mass star-forming regions. Note that only the high-mass protostellar objects and starless clumps (HMPO and HMSC, respectively), and IRDCs are plotted from the surveys of Fontani et al. (2011) and Gerner et al. (2015). The lines overlaid represent deuterium fractions of $D_{frac}^{N_2H^+} = [0.001, 0.01, 0.04, 0.1, 1.0]$ from right to left, respectively.

2015b) and low-mass (triangles only; Crapsi et al. 2005; Friesen et al. 2010, 2013) cores described within the literature.

We find that our deuterium fractions are most similar to those found in IRDCs by Gerner et al. (2015), who found mean values of ∼0.01–0.1 (observed at spatial resolution of a ∼few 10 arcsec, at ∼4 kpc). However, our values are an order of magnitude lower than the values observed by Fontani et al. (2011) and Kong et al. (2015b) towards high-mass starless cores (HMSCs), where $D_{frac}^{N_2H^+} \sim 0.3$. Gerner et al. (2015) suggest that the low deuteration values found in their sample of IRDCs may be due to the presence of unresolved evolved objects (24 μm sources). This could also be the case for G035.39−00.33, as the average deuterium fraction is also close

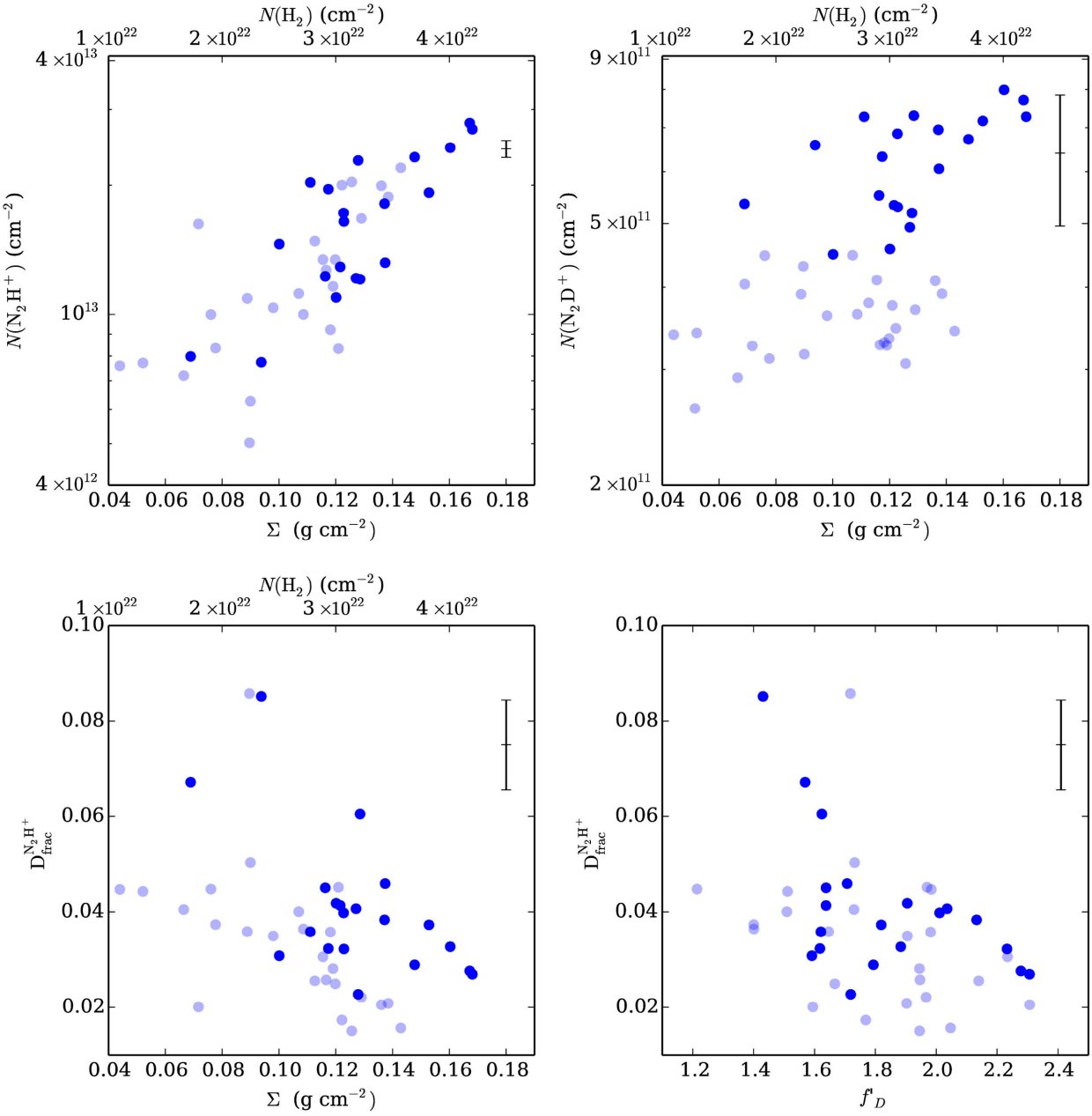

Figure 5. Shown in the panels are the N_2H^+ (upper left) and N_2D^+ (upper right) column densities as a function of mass surface density, deuterium fraction as a function of mass surface density (lower left), and deuterium fraction as a function of normalized CO depletion factor (lower right). Average errors for N_2D^+column density and $D_{frac}^{N_2H^+}$ are displayed in the upper right of each plot. Not shown are the errors on the mass surface density and CO depletion, which are ∼30 per cent (Kainulainen & Tan 2013) and ∼50 per cent (Paper III), respectively. The solid and transparent points represent positions where both the N_2H^+ and N_2D^+ emission is above a 3σ and 2σ error threshold, respectively.

to the values observed towards high-mass protostellar candidates (∼0.04; Fontani et al. 2006, 2011).

To investigate how the $N_2H^+$and N_2D^+ emission and the deuterium fraction vary within G035.39−00.33, we plot them as a function of mass surface density in Fig. 5. If we consider only the positions above a 3σ error threshold, the column density of N_2D^+ remains relatively constant with increasing mass surface density (dynamical range of ∼1.5, which is similar to the scale of the uncertainties). However, for the same positions, the column density of N_2H^+ shows a significant positive gradient with increasing mass surface density (dynamical range of ∼3). This is reflected in the plot of deuterium fraction as a function of mass surface density, which shows an overall negative correlation. This is consistent with a picture in which the N_2D^+ is more spatially concentrated in cores than the N_2H^+, which is also present in the clump envelope (that dominates the mass).

Observations show that the deuterium fraction is highly sensitive to the level of CO freeze-out (e.g. Caselli et al. 2002a), where the CO depletion factor, f_D, can be expressed as the ratio of the observed mass surface density to mass surface density derived from CO emission, assuming a reference CO fractional abundance with respect to H_2. Paper III calculated the CO depletion averaged along

each line of sight (i.e. each pixel) throughout G035.39−00.33, f'_D, which is normalized such that on average pixels with mass surface densities of 0.01 g cm^{-2} < Σ <0.03 g cm^{-2} are unity. Fig. 5 displays the deuterium fraction as a function of normalized CO depletion factor, for which we do not see a positive correlation, but rather again an anticorrelation. This is contrary to what is expected, that level of deuteration is elevated in dense, CO depleted cores; but it is reminiscent of the results recently obtained towards the Ophiuchus low-mass star-forming region (Punanova et al. 2015). These authors suggest that the highly deuterated but CO-rich cores may be recently formed, centrally concentrated starless cores.

These results could indicate that along the line of sight, high-mass surface density and CO depleted positions have enhanced N_2H^+, but the N_2D^+ is only tracing a portion of this in the 3rd dimension. We, therefore, suggest that measurements of the deuterium fraction in massive star-forming regions could be limited by low spatial resolution observations (beam dilution), and/or the relatively unknown evolutionary stage of the gas (whether or not it has reached chemical equilibrium or is being influenced by the presence of young stellar objects). These are discussed in more detail in the following section.

5.2 Comparison with chemical models

To determine if the observed levels of deuteration are consistent with the current evolutionary stage of the G035.39−00.33, we have conducted a series of chemical models (Kong et al. 2015a). The model consists of the NAHOON code and a reduced network extracted from KIDA data base (Wakelam et al. 2012), including the elements H, D, He, C, N, O. The chemical species traced by the code contain up to three atoms in size, except for H_3O^+ and its deuterated isotopologues, which significantly improve the consistency with a more complete network (Sipilä et al. 2013). Spin states of H_2, H_3^+ and their deuterated isotopologues are included, and the formation of o-H_2, p-H_2, HD, o-D_2, p-D_2 on dust grain surface are considered following Le Petit, Roueff & Le Bourlot (2002). We follow Pagani et al. (2009a) in calculating the dissociative recombination rates of all forms of H_3^+. The initial elemental abundances are listed in table 2 in Kong et al. (2015a). In this paper, we treat the depletion of neutral species by reducing the initial elemental abundances of C, N, O by the depletion factor, f_D, and consider a broad combination of physical conditions appropriate for IRDC G035.39−00.33.

We explore a grid of models with A_v = [5, 10, 20, 30] mag, n_H = [0.1, 1, 2, 10] × 10^4 cm^{-3}, T_{kin} = [10, 15, 20] K, f_D = [1, 2, 3, 5, 10], to check the equilibrium $D_{frac}^{N_2H^+}$ and time-scale. We adopt a constant radiation field four times stronger than the standard Habing field (G_0), however because of high visual extinction values considered here, small changes of G_0 do not affect the chemistry. We also explore initial ortho-to-para H_2 ratios of $OPR_0^{H_2}$ = 0.001–3. A $OPR_0^{H_2}$ = 3 represents the high temperature statistical ratio limit, as ortho- and para-H_2 are formed at high temperatures on dust grains in the ratio of their nuclear spin state statistical weights (3:1; Flower 2003). $OPR_0^{H_2}$ = 0.1–1 are values close to those deduced by Crabtree et al. (2011) in translucent clouds with T = 50–70 K: 0.8–0.3. Recently, Xu et al. (2016) made some rough constraints on the H_2 ortho-to-para ratio for the low-density gas within Taurus. These authors estimate OPR^{H_2} ∼ 0.2. Lower values are expected in dark molecular clouds (see Sipilä et al. 2013). Therefore, our $OPR_0^{H_2}$ exploration covers typical values observed in molecular clouds.

Table 2 presents the results of a subset of models with input parameters which best represent the global properties of G035.39−00.33. Shown are the equilibrium deuterium fraction, $D_{frac,eq}^{N_2H^+}$, the time taken to achieve 90 per cent of this value. Variation of the extinction is not displayed in the table, as ranging A_v between [10, 20, 30] mag does not significantly affect the results, however an extinction of 5 mag tends to decrease the $D_{frac,eq}^{N_2H^+}$ and the time by a factor of a few. This is not thought to be an issue as the mapped region of G035.39−00.33 has an average extinction of ∼20 mag (Kainulainen & Tan 2013).

The observed deuterium fractions within G035.39−00.33 are generally similar with the model equilibrium values, for kinetic temperatures of 10 and 15 K. If we assume that the cloud has a mean global density n_H ∼10^4 cm^{-3} (Paper III), a mean CO depletion of f_D = 3, and assume the mean kinetic temperature is comparable to the ∼15 K dust temperature found by Nguyen Luong et al. (2011), the model predicted equilibrium value is $D_{frac,eq}^{N_2H^+}$ = 0.048, remarkably close to the average observed value of $D_{frac}^{N_2H^+}$ = 0.04 ± 0.01.

Fig. 6 shows how the ortho-to-para ratio of H_2 and $D_{frac}^{N_2H^+}$ vary as a function of time, for the model parameters of n_H = 10^4 cm^{-3}, f_D = 3, T_{kin} = 15 K, and A_v = 20 mag. For these properties which best describe G035.39−00.33, we find the time reach the observed deuterium fraction vary between ∼0.2 and 8 Myr, where the shortest times are for low initial ortho-to-para ratios (e.g. $OPR_0^{H_2}$ = 0.001; also see Table 2).

Fig. 7 displays the time needed to reach the observed deuterium fraction of $D_{frac}^{N_2H^+}$ = 0.04 from a given initial ortho-to-para ratio of H_2 (shown on the top axis) versus the time needed to reach this initial ortho-to-para ratio if starting from the high temperature statistical ratio limit of 3 (Kong et al. 2015a). The solid blue line shows this result for the fiducial model parameters, e.g. of density, temperature, depletion factor, cosmic ray ionization rate. The dashed blue line shows the time to reach $D_{frac}^{N_2H^+}$ = 0.02 for the fiducial model.

An estimate of the total age of the molecular cloud, i.e. from the time when the molecules formed with an assumed high temperature statistical ratio limit of 3 until the time they achieve the observed deuteration level, is the sum of the ortho-to-para ratio decay time-scale and deuteration time-scale: example contours of this sum for 0.3, 1, 3, 10 Myr are shown by the dotted black lines. The astrochemical model results indicate that a time-scale of at least 3 Myr is needed for the cloud to evolve from its initial state to the present observed deuterated state. Adopting values of CO depletion factor and density of a factor 2 higher (f_D = 6 and n_H = 2 × 10^4 cm^{-3}) or a cosmic ionization rate of a factor 2 lower (ζ = 1.25 × 10^{-17} s^{-1}) would imply cloud ages of at least 3–7 Myr, shown in lower panel of Fig. 7. We note that decreasing the CO depletion or density, or increasing the cosmic ionization rate would cause the models to never reach an equilibrium deuterium fraction of 0.04, hence these are not plotted on Fig. 6. We thus conclude that the age of IRDC G035.39−00.33 is at least ∼3 Myr. This is a lower limit, since the current observed deuteration level is consistent with astrochemical equilibrium.

A lower limit of 3 Myr is equivalent to ∼8 local free-fall time-scales, assuming an average density of 10^4 cm^{-3} (with spherical geometry ∼4 × 10^5 yr). This indicates the cloud is dynamically 'old' and is thus likely to have had time to achieve approximate virial equilibrium (as was concluded in Paper III). This time-scale is consistent with that estimated from a kinematic analysis in Paper IV. We note that future studies will involve comparison with models of evolving density (i.e. an evolving free-fall time).

Table 2. Equilibrium deuterium fractions for models with an extinction of $A_v = 20$ mag, number densities, n_H, of 10^4 and 10^5 cm^{-3}, and initial ortho-to-para H_2 ratios of 0.001, 0.01, 0.1, and 1. Columns show the model inputs of gas kinetic temperature, T_{kin}, CO depletion, and model outputs of equilibrium value of $D_{frac}^{N_2H^+}$ and the time taken to achieve 90 per cent of this value, $t_{eq,\,90}$.

T_{kin} (K)	f_D	$D_{frac,eq}^{N_2H^+}$	$t_{eq,\,90}$ (Myr)			
			$OPR_0^{H_2} = 0.001$	$OPR_0^{H_2} = 0.01$	$OPR_0^{H_2} = 0.1$	$OPR_0^{H_2} = 1$
			$n_H = 10^4$ cm^{-3} ($t_{ff} = 4.4 \times 10^5$ yr)			
10.0	1.0	0.021	0.73	3.24	6.19	8.36
10.0	3.0	0.044	0.29	2.10	3.61	4.73
10.0	5.0	0.057	0.24	1.79	3.01	3.92
10.0	10.0	0.076	0.26	1.50	2.45	3.16
15.0	1.0	0.022	0.71	3.32	6.32	8.50
15.0	3.0	0.048	0.27	2.06	3.52	4.60
15.0	5.0	0.062	0.20	1.73	2.90	3.76
15.0	10.0	0.083	0.19	1.43	2.32	2.99
20.0	1.0	0.015	0.39	2.91	6.48	8.72
20.0	3.0	0.025	0.03	1.90	3.57	4.65
20.0	5.0	0.029	0.003	1.61	2.91	3.76
20.0	10.0	0.034	0.0005	1.32	2.32	2.96
			$n_H = 10^5$ cm^{-3} ($t_{ff} = 1.4 \times 10^5$ yr)			
10.0	1.0	0.026	0.67	2.87	5.23	6.99
10.0	3.0	0.076	0.45	1.48	2.35	3.02
10.0	5.0	0.111	0.40	1.13	1.75	2.23
10.0	10.0	0.17	0.40	0.84	1.28	1.61
15.0	1.0	0.027	0.65	2.96	5.44	7.27
15.0	3.0	0.079	0.32	1.48	2.37	3.04
15.0	5.0	0.115	0.29	1.12	1.74	2.21
15.0	10.0	0.175	0.28	0.83	1.26	1.58
20.0	1.0	0.017	0.35	2.67	5.69	7.61
20.0	3.0	0.033	0.06	1.45	2.49	3.18
20.0	5.0	0.04	0.01	1.09	1.81	2.28
20.0	10.0	0.048	0.0004	0.79	1.27	1.59

Given that much of the complex structure observed in the mass surface density plot is not seen in the N_2D^+ and N_2H^+ emission maps, it is interesting to question if we are resolving all the dense sub-structures. Core diameters extracted from 3.2 mm continuum observations of G035.39−00.33 with the PdBI are typically 0.1 pc (Henshaw et al., in preparation). This implies an approximate beam dilution factor of ∼0.07 (i.e. the square of the core-to-beam size ratio). To check this, we input typical core properties in the model. Assuming the cores have densities of $\sim 10^5$ cm^{-3} (average 'core'; e.g. Butler & Tan 2012), temperatures of ∼10 K, and CO depletions of ∼5–10, we find model predicted $D_{frac,eq}^{N_2H^+}$ of 0.11–0.17 (see Table 2), which are closer to the deuteration values found in high-mass pre-stellar cores (Fontani et al. 2011). Applying the beam dilution factor to the predicted values, we find deuterium fractions of ∼0.007–0.01. Although these values are slightly below what is observed, this could be a plausible explanation for the low observed deuterium fractions in the IRDCs, where unresolved dense cores are present. The time-scales to reach these deuteration levels in gas at these higher densities of 10^5 cm^{-3} are shorter: ∼1 Myr (see also Punanova et al. 2015). However, this is still long compared to the local free-fall time of ∼0.1 Myr.

Higher angular resolution observations of N_2D^+ are needed to disentangle if G035.39−00.33 has reached a deuterium fraction equilibrium in its diffuse, $\sim 10^4$ cm^{-3} bulk density, or if the observed deuteration is dominated by a population of denser, currently unresolved cores.

6 SUMMARY

In this work, we have presented N_2D^+ (2 − 1) data towards G035.39−00.33. The main results are summarized below.

(i) The emission from N_2D^+ is extended across G035.39−00.33, and from this emission we calculate a mean beam-averaged column density of $N(N_2D^+) = 6.2 \pm 1.4 \times 10^{11}$ cm^{-2}.

(ii) We report an average deuterium fraction of $D_{frac}^{N_2H^+}$ (N_2D^+/N_2H^+) = 0.04 ± 0.01, which is three orders of magnitude higher than the interstellar [D]/[H] ratio, and within the range quoted for other IRDCs (e.g. Miettinen et al. 2011; Gerner et al. 2015), yet it is significantly smaller than the values found towards massive starless cores within quiescent IRDCs (Fontani et al. 2011).

(iii) We have conducted chemical modelling of the deuteration, and find that the observed values of the deuterium fraction are consistent with those of chemical equilibrium. Such an equilibrium would have taken at least ∼3 Myr to be established. This scenario places a lower limit on the cloud age of ∼8 local free-fall times, which indicates that the IRDC filament is dynamically 'old', with sufficient time to relax to a quasi-equilibrium virialized state. This is consistent with the previous age estimates based on the kinematics (Paper IV). Future studies will involve comparison with models of evolving density (i.e. an evolving free-fall time).

(iv) To test if beam dilution of denser unresolved substructure is causing the low deuterium fraction, we input typical core properties in the model. We find that these would reach

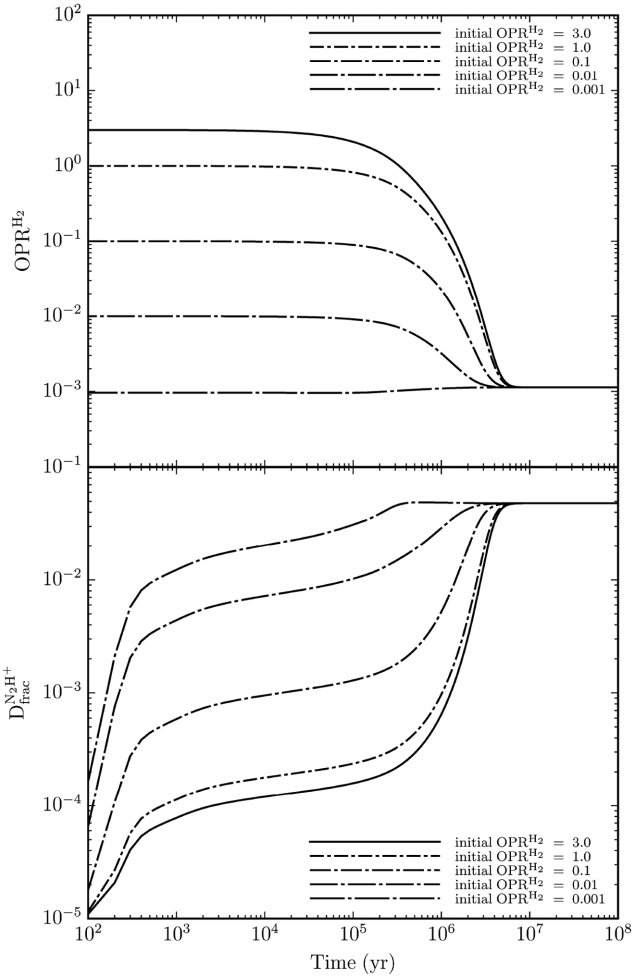

Figure 6. Time evolution of the OPR^{H_2} (upper panel) and $D_{frac}^{N_2H^+}$ (lower panel) under different assumptions of the initial OPR^{H_2}, for $n_H = 10^4$ cm^{-3}, $f_D = 3$, $T_{kin} = 15$ K, and $A_v = 20$ mag. We explore OPR^{H_2} from 3 down to 0.001.

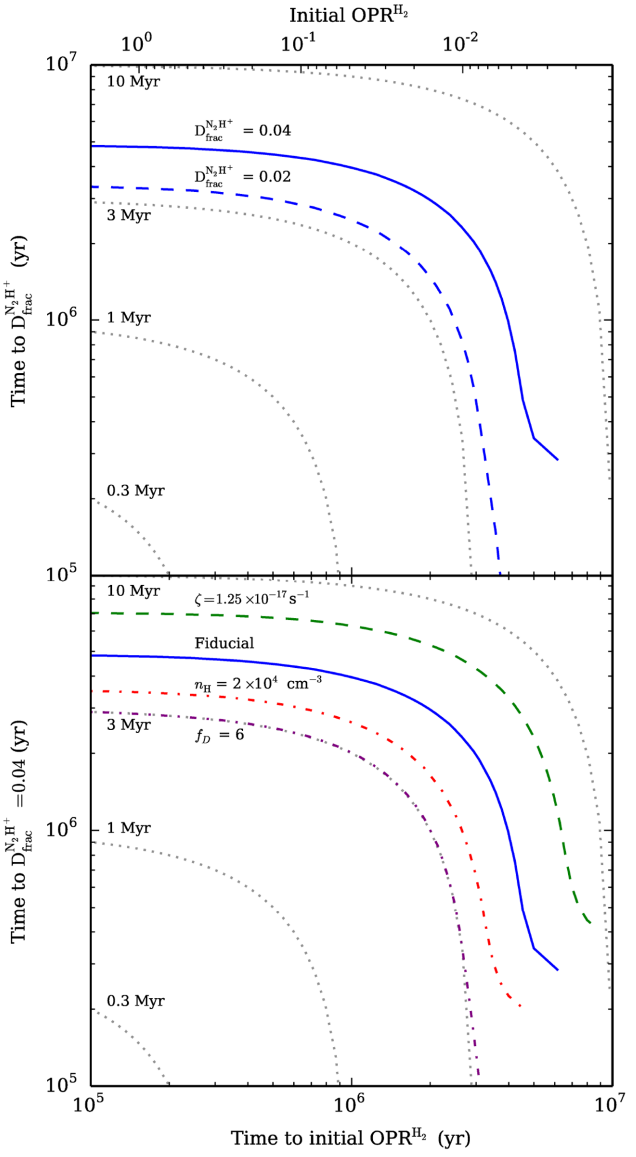

Figure 7. Time to reach the observed deuterium fraction ($D_{frac}^{N_2H^+} = 0.04$) from a given initial ortho-to-para ratio of H_2 (shown on the top axis) versus the time to reach this initial ortho-to-para ratio if starting from statistical equilibrium ratio of 3. The solid blue line shows this result for the fiducial model parameters, e.g. of density, temperature, depletion factor, cosmic ray ionization rate. Grey dotted lines show contours of the sum of the deuteration time-scale and ortho-to-para ratio decay time-scale to equal 0.3, 1, 3, 10 Myr, as labeled. The dashed blue line (upper panel) shows the time to reach $D_{frac}^{N_2H^+} = 0.02$ for the fiducial model. The dashed and dot–dashed lines (lower panel) show the effect of varying several of the model parameters, as labeled.

equilibrium faster (in about 1 Myr) and have a higher equilibrium value. Using estimates for the cores size, of ∼0.1 pc, we determine that a beam dilution factor of ∼0.07 is needed to reproduce the observed deuterium fractions, i.e. dense cold cores only occupy 7 per cent of the cloud volume. Note that, irrespective of this, the cloud is still dynamically old.

In light of the results, we propose that higher angular resolution observations are needed to further investigate the nature of the deuterium fraction measured across G035.39−00.33.

ACKNOWLEDGEMENTS

We have completed this paper based on observations carried out with the IRAM 30 m Telescope. IRAM is supported by INSU/CNRS (France), MPG (Germany), and IGN (Spain). We would like to thank the anonymous referee for their constructive comments. Furthermore, we would like to thank Michael Butler and Jouni Kainulainen for providing us with the mass surface density map, and Audra Hernandez for the CO depletion factor map. This research has made use of NASA's Astrophysics Data System. ATB would like to acknowledge the funding provided by Liverpool John Moores University, Max-Plank-Institute for Extraterrestrial Physics, and the University of Leeds. PC acknowledges the financial support of the European Research Council (ERC; project PALs 320620). IJ-S acknowledges the funding received from the STFC through an Ernest Rutherford Fellowship (proposal number ST/L004801/1). JCT acknowledges NASA grant ADAP10-0110.

REFERENCES

Belloche A., Parise B., van der Tak F. F. S., Schilke P., Leurini S., Güsten R., Nyman L.-Å., 2006, A&A, 454, L51

Bergin E. A., Tafalla M., 2007, ARA&A, 45, 339
Bergin E. A., Alves J., Huard T., Lada C. J., 2002, ApJ, 570, L101
Bourke T. L., Myers P. C., Caselli P., Di Francesco J., Belloche A., Plume R., Wilner D. J., 2012, ApJ, 745, 117
Butler M. J., Tan J. C., 2012, ApJ, 754, 5
Carey S. J. et al., 2009, PASP, 121, 76
Caselli P., Walmsley C. M., Tafalla M., Dore L., Myers P. C., 1999, ApJ, 523, L165
Caselli P., Walmsley C. M., Zucconi A., Tafalla M., Dore L., Myers P. C., 2002a, ApJ, 565, 344
Caselli P., Benson P. J., Myers P. C., Tafalla M., 2002b, ApJ, 572, 238
Cazzoli G., Puzzarini C., Lapinov A. V., 2003, ApJ, 592, L95
Chambers E. T., Jackson J. M., Rathborne J. M., Simon R., 2009, ApJS, 181, 360
Clemens D. P., 1985, ApJ, 295, 422
Crabtree K. N., Indriolo N., Kreckel H., Tom B. A., McCall B. J., 2011, ApJ, 729, 15
Crapsi A., Caselli P., Walmsley C. M., Tafalla M., Lee C. W., Bourke T. L., Myers P. C., 2004, A&A, 420, 957
Crapsi A. et al., 2005, A&A, 439, 1023
Dalgarno A., Lepp S., 1984, ApJ, 287, L47
di Francesco J., Evans N. J., II, Caselli P., Myers P. C., Shirley Y., Aikawa Y., Tafalla M., 2007, in Reipurth B., Jewitt D., Keil K., eds, Protostars and Planets V. Univ. Arizona Press, Tucson, AZ, p. 17
Dore L., Caselli P., Beninati S., Bourke T., Myers P. C., Cazzoli G., 2004, A&A, 413, 1177
Flower D., 2003, Molecular Collisions in the Interstellar Medium. Cambridge Univ. Press, Cambridge
Fontani F., Caselli P., Crapsi A., Cesaroni R., Molinari S., Testi L., Brand J., 2006, A&A, 460, 709
Fontani F. et al., 2011, A&A, 529, L7
Fontani F., Palau A., Busquet G., Isella A., Estalella R., Sanchez-Monge Á., Caselli P., Zhang Q., 2012a, MNRAS, 423, 1691
Fontani F., Giannetti A., Beltrán M. T., Dodson R., Rioja M., Brand J., Caselli P., Cesaroni R., 2012b, MNRAS, 423, 2342
Fontani F., Caselli P., Zhang Q., Brand J., Busquet G., Palau A., 2012c, A&A, 541, A32
Friesen R. K., Di Francesco J., Myers P. C., Belloche A., Shirley Y. L., Bourke T. L., André P., 2010, ApJ, 718, 666
Friesen R. K., Kirk H. M., Shirley Y. L., 2013, ApJ, 765, 59
Gerner T., Shirley Y., Beuther H., Semenov D., Linz H., Abertsson T., Henning T., 2015, A&A, 579, A80
Giannetti A. et al., 2014, A&A, 570, A65
Henshaw J. D., Caselli P., Fontani F., Jiménez-Serra I., Tan J. C., Hernandez A. K., 2013, MNRAS, 428, 3425 (Paper IV)
Henshaw J. D., Caselli P., Fontani F., Jiménez-Serra I., Tan J. C., 2014, MNRAS, 440, 2860 (Paper VI)
Hernandez A. K., Tan J. C., Caselli P., Butler M. J., Jiménez-Serra I., Fontani F., Barnes P., 2011, ApJ, 738, 11 (Paper II)
Hernandez A. K., Tan J. C., Kainulainen J., Caselli P., Butler M. J., Jiménez-Serra I., Fontani F., 2012, ApJ, 756, L13 (Paper III)
Jiménez-Serra I., Caselli P., Tan J. C., Hernandez A. K., Fontani F., Butler M. J., van Loo S., 2010, MNRAS, 406, 187 (Paper I)
Jiménez-Serra I., Caselli P., Fontani F., Tan J. C., Henshaw J. D., Kainulainen J., Hernandez A. K., 2014, MNRAS, 439, 1996 (Paper V)
Kainulainen J., Tan J. C., 2013, A&A, 549, A53
Kong S., Caselli P., Tan J. C., Wakelam V., Sipilä O., 2015a, ApJ, 804, 98
Kong S., Tan J. C., Caselli P., Fontani F., 2015b, preprint (arXiv:1511.02100)
Kutner M. L., Ulich B. L., 1981, ApJ, 250, 341
Le Petit F., Roueff E., Le Bourlot J., 2002, A&A, 390, 369
Miettinen O., Hennemann M., Linz H., 2011, A&A, 534, A134
Millar T. J., Bennett A., Herbst E., 1989, ApJ, 340, 906
Nguyen Luong Q. et al., 2011, A&A, 535, A76
Oliveira C. M., Hébrard G., Howk J. C., Kruk J. W., Chayer P., Moos H. W., 2003, ApJ, 587, 235
Pagani L., Salez M., Wannier P. G., 1992, A&A, 258, 479
Pagani L., Bacmann A., Cabrit S., Vastel C., 2007, A&A, 467, 179
Pagani L. et al., 2009a, A&A, 494, 623
Pagani L., Daniel F., Dubernet M., 2009b, A&A, 494, 719
Punanova A., Caselli P., Pon A., Belloche A., André P., 2015, preprint (arXiv:1512.02986)
Ragan S. E., Bergin E. A., Wilner D., 2011, ApJ, 736, 163
Rathborne J. M., Jackson J. M., Simon R., 2006, ApJ, 641, 389
Simon R., Rathborne J. M., Shah R. Y., Jackson J. M., Chambers E. T., 2006, ApJ, 653, 1325
Sipilä O., Caselli P., Harju J., 2013, A&A, 554, A92
Tan J. C., Beltrán M. T., Caselli P., Fontani F., Fuente A., Krumholz M. R., McKee C. F., Stolte A., 2014, in Beuther H., Klessen R. S., Dullemond C. P., Henning T., eds, Protostars and Planets VI. Univ. Arizona Press, Tucson, AZ, p. 149
Wakelam V. et al., 2012, ApJS, 199, 21
Walmsley C. M., Flower D. R., Pineau des Forêts G., 2004, A&A, 418, 1035
Xu D., Li D., Yue N., Goldsmith P. F., 2016, preprint (arXiv:1601.03165)

This paper has been typeset from a TEX/LATEX file prepared by the author.